

UNIVERSITY OF TORONTO

Modelling of *d*-wave Tunnelling Devices and Proximity Effect

by

Jianwei Xu

A thesis submitted in partial fulfillment for the
degree of Master of Science

in the
Faculty of Arts & Science
Department of Physics

August 2012

UNIVERSITY OF TORONTO

Abstract

Faculty of Arts & Science

Department of Physics

Master of Science

by [Jianwei Xu](#)

In this thesis we are interested in the calculation of the tunnelling spectroscopy.

First of all, we discuss explicitly the calculation based on the BTK theory. The analytic formula of the differential conductance is stated. Then we move to the theory of the tunnelling spectroscopy where we emphasize the d -wave modelling, including the topics of ab -tunnelling and c -tunnelling spectroscopy. Also, we apply our model to fit the data of our BSCCO on BSC experiments. What is more, the popular genetic algorithm for fitting the results is introduced.

Also, we attempt to study the unconventional proximity effect. A brief approach to calculate the Bogoliubov equation is presented. And the properties of the s -wave and d -wave ab tunnelling spectroscopy affected by the reduced and induced gaps are studied.

Acknowledgements

Thanks for the priceless help from my supervisor, Prof. Ken Burch, and all the people who helped me. . .

Contents

Abstract	i
Acknowledgements	ii
1 Introduction	1
2 Tunnelling Spectroscopy of D-Wave Superconductors	3
2.1 Properties of Energy Gaps	3
2.1.1 Pair Potential of Anisotropic Superconductors	4
2.1.2 Energy Gap Terms Selected for the Calculation	5
2.2 D -Wave Tunnelling Spectroscopy of Superconductors	5
2.2.1 I-V Curve Function For N-S Boundary	6
2.2.2 Properties of Tunnelling Spectroscopy Kernel σ_S	6
2.2.3 ab -Tunnelling Spectroscopy	8
2.2.4 Differential Conductance with Different Temperatures and Fixed Energy Gap Amplitude	10
2.2.5 Differential Conductance with Different Pair Potential Amplitudes with Fixed Temperature	11
2.2.6 c -Tunnelling Spectroscopy and Fitting the Experimental Data . . .	13
3 Tunnelling Spectroscopy with Proximity Effect	17
3.1 Bogoliubov Equations	17
3.1.1 Simplification for the Bogoliubov Equations	18
3.1.2 Solving the Bogoliubov Equations	19
3.2 Properties of Tunnelling Spectroscopy Kernel with Proximity Effect at Normal Incident	22
3.2.1 The Shapes of Reduced and Induced Pair Potential	22
3.2.2 Specific Cases	23
3.2.3 s -wave Proximity Effect at Normal Incident with Various Parameters	23
3.3 An In Progress Approach to the d -wave Tunnelling Spectroscopy with Proximity Effect	26
4 Future Work	33
5 Additional Projects	34
5.1 Control System for Raman Stage and Fresnel Rhomb	34

Chapter 1

Introduction

Tunnelling spectroscopy of superconductors is a heavily studied topic. The typical experimental results are modelled based on the work of Blonder, Tinkham, and Klapwijk (BTK) [1] who proposed a theory focusing on the tunnelling spectroscopy between a normal metal and a conventional *s*-wave superconductor. Extension of the theory, however, should be explored as in BTK, the calculation of tunnelling spectroscopy is for simple *s*-wave case. Also, the assumed step function of pair potential should be questioned. In addition, there are newly conducted experiments, showing some new features of the tunnelling spectroscopy [2–4].

One extension of the BTK theory discussed by various authors [5–7] is to establish theory of the *d*-wave tunnelling spectroscopy, which is required by various experiments [8, 9]. Another more advanced approach is to include the proximity effect, where we need to numerically solve the Bogoliubov equations due to the increased complexity of having a spatially dependent superconducting gap [3, 10, 11]. Previous theoretical studies of the superconducting proximity effect, however, were limited primarily to *s*-wave superconductors, as it was believed to be exceedingly difficult to generate a proximity effect with the high temperature superconductors. Nonetheless this long held belief was recently shown to be incorrect by our groups newly invented mechanical bonding technique. To get a better understanding of our experimental results in our group, it is necessary to establish a *d*-wave tunnelling spectroscopy theory accounting for proximity effect, which has not been clearly discussed before. This thesis discusses our recent effort to approach the simulation of this effect by establishing the model of proximity tunnelling spectroscopy.

The general approach always follows the following steps. First, we write the Hamiltonian for the material, from which we derive the function of the pair potential. Second, we solve the Bogoliubov equations with assumptions and the obtained pair potential, from which

we get the so called tunnelling conductance kernel for a specific solid angle. Third, the integration over the half-fermi sphere is conducted so that we get the total tunnelling conductance. Forth, the total tunnelling conductance joins the convolution with the differential fermi distribution function. With the previous model established, we apply some additional algorithms like genetic algorithm to fit the experimental data.

Chapter 2

Tunnelling Spectroscopy of *D*-Wave Superconductors

2.1 Properties of Energy Gaps

The Hamiltonian of the interaction in a superconductor based on weak coupling BCS theory is generally modelled as

$$H_{eff} = \sum_{k,k'} V(\mathbf{k}, \mathbf{k}') C_{k'}^+ C_{-k'}^+ C_{-k} C_k \quad (2.1)$$

where $V(\mathbf{k}, \mathbf{k}')$ represents the attractive potential between carriers, $C_{k'}^+$ electron creator, and C_k annihilator of k electron. As shown originally by Bardeen, Cooper and Schrieffer this not only binds the electrons into cooper pairs, but results in their condensate. However a consequence of the formation of the condensate is an energy gap in the single particle spectrum whose size is given by:

$$\Delta(k) = - \sum_{k'} V(\mathbf{k}, \mathbf{k}') \langle C_{-k'} C_{k'} \rangle \quad (2.2)$$

The key difference between an isotropic superconductor and an anisotropic superconductor is their \mathbf{k} space dependence of the potential, $V(\mathbf{k}, \mathbf{k}')$. In a conventional superconductor the gap is independent of momentum, whereas in an unconventional superconductor the gap acquires a k -dependence.

2.1.1 Pair Potential of Anisotropic Superconductors

When dealing with anisotropic superconductors, the interaction is no longer \mathbf{k} space independent, leading to the fact that we have to change the form of the pair potential. Assuming that the interaction is only determined by the angle between \mathbf{k}, \mathbf{k}' and expanding the interaction we get,

$$V_{kk'} = V(\mathbf{k} \cdot \mathbf{k}') = V(\cos \theta_{kk'}) = \sum_l (2l+1) V_l P_l(\cos \theta_{kk'}) \quad (2.3)$$

where P_l are the Legendre Functions, in which

$$V_l = \frac{1}{2} \int_{FS} \frac{d\Omega}{4\pi} V_{kk'} P_l(\cos \theta_{kk'}) \quad (2.4)$$

Notice that the integral is limited to the fermi surface. Through dynamic Green function we could derive that

$$\Delta(\hat{\mathbf{k}}, T) = \Delta_a(T) \sqrt{4\pi} \sum_{m=-l}^l a_m Y_{lm}(\theta, \phi) \quad (2.5)$$

where Y_{lm} are spherical harmonics. The average $\Delta_a(T)$ over \mathbf{k} satisfies

$$1 = \frac{1}{2} |V_l| \sum_{k'} 4\pi \left| \sum_{m=-l}^l a_m Y_{lm}(\hat{k}') \right|^2 \frac{\tanh(\frac{1}{2}\beta\epsilon_{k'})}{\epsilon_{k'}} \quad (2.6)$$

where

$$\Delta_{k'} = \sqrt{\epsilon_{k'}^2 + 4\pi \Delta_a^2(T) \left| \sum_{m=-l}^l Y_{lm}(\hat{\mathbf{k}}) \right|^2} \quad (2.7)$$

Similar to the BCS theory, we replace the sum operator with integral

$$\sum_k = \int d\Omega \int_0^{\hbar\omega} d\epsilon = \int_0^{2\pi} d\phi \int_0^\pi \sin \theta d\theta \int_0^{\hbar\omega} d\epsilon \quad (2.8)$$

We could get the equation

$$1 = N(0) |V_L| \int d\Omega \int_0^{\hbar\omega} d\epsilon \frac{4\pi |Y_{lm}(\theta, \phi)|^2 \tanh(\frac{1}{2}\beta\epsilon)}{\epsilon} \quad (2.9)$$

2.1.2 Energy Gap Terms Selected for the Calculation

If we fix the temperature, only the formal solution(2.5) is used, in which we treat term $\Delta_a(T)$ as a constant. Therefore, for s -wave,

$$\Delta(\hat{\mathbf{k}}, T) = \Delta_a(T) \sqrt{4\pi} Y_{00}(\theta, \phi) = \Delta_a(T) \sqrt{4\pi} \cdot \frac{1}{2} \sqrt{\frac{1}{\pi}} \sim \Delta_0 \quad (2.10)$$

and for d -wave we limit our discussion to $d_{x^2-y^2}$ corresponding to the symmetry of high T_c cuprates in two dimensional Brillouin zone, we have,

$$\Delta \sim Y_{2,-2}(\theta, \phi) + Y_{2,2}(\theta, \phi) \sim \frac{1}{4} \sqrt{\frac{15}{2\pi}} \left(\sin^2 \theta e^{-2\phi} + \sin^2 \theta e^{2\phi} \right) \Big|_{\theta=\frac{\pi}{2}} \sim \Delta_0 \cos(2\phi) \quad (2.11)$$

As shown in Fig.2.1. A key difference between the two is the change in sign of the order parameter in the d -wave case. However since we are generally concerned with tunnelling along the c -axis, this anisotropy generally is only revealed through the well known V-Shape of the conductance spectra (due to averaging over the gap values).

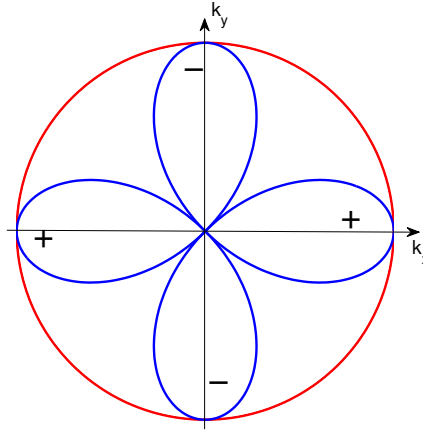


FIGURE 2.1: The shape of s -wave energy gap is a circle while that of d -wave energy gap is like a petal. Notice that the $d_{x^2-y^2}$ has two positive and negative leaves

2.2 D -Wave Tunnelling Spectroscopy of Superconductors

To approach the calculation of tunnelling spectroscopy of superconductors to fit the experimental results in our group, there are several steps to go in both theory and calculation. First of all, we need to establish the model for s -wave, the basis for the following calculations. Second, s -wave model serves the kernel so that it will guide us

to the d-wave tunnelling spectroscopy results by conducting an integral over it. Finally, we obtain the conductances that can be compared to our BSCCO on BSC experiments. In addition, an algorithm for fitting the results is implemented.

We first introduce the formula for the conductance versus bias[1] before we discuss the details of the d-wave tunnelling spectroscopy.

2.2.1 I-V Curve Function For N-S Boundary

The reference[1] derives that the I-V curve for N-S Boundary could be written like

$$I_{NS} = 2N(0)ev_F\mathcal{A} \int_{-\infty}^{\infty} [f_0(E - eV) - f_0(E)][1 + A(E) - B(E)]dE \quad (2.12)$$

in which $f_0(E)$ is the fermi distribution and $B(E)$ is the probability of normal reflection and $A(E)$ is the probability of Andreev reflection, namely where the electron enters the superconductor as a cooper pair, while reflecting a hole.

$$f_0(E) = \frac{1}{1 + e^{(E-\mu)/kT}} \quad (2.13)$$

where μ is the chemical potential. By applying a differential operation on (2.12) we get that

$$\sigma = \frac{\partial I}{\partial V} = \int_{-\infty}^{\infty} \sigma_T(E) \frac{\partial f_0(E - eV)}{\partial V} dE \quad (2.14)$$

Omitting the constant factor, the following term is what we are focusing on

$$\begin{aligned} \sigma_T(E) &= \int d\Omega \sigma_S \cos \theta = \int d\Omega (1 + A(E) - B(E)) \cos \theta \\ \sigma_S(E) &= 1 + A(E) - B(E) \end{aligned} \quad (2.15)$$

where $A(E)$ is the famous Andreev reflection and $B(E)$ is the ordinary reflection, and θ is the incident angle since we are only considering the current along the tunnelling axis[1], the former of which reflects a hole and generate a Cooper pair in the superconductor side.

2.2.2 Properties of Tunnelling Spectroscopy Kernel σ_S

Let's first study the tunnelling spectroscopy kernel σ_S shown in (2.15).

The Bogoliubov equations can be analytically solved if we assume that the potential between the two materials is a δ function while energy gap is a step function [5], demonstrated in Fig.2.2. Also we define the effective pair potential Δ_+ felt by the electron-like

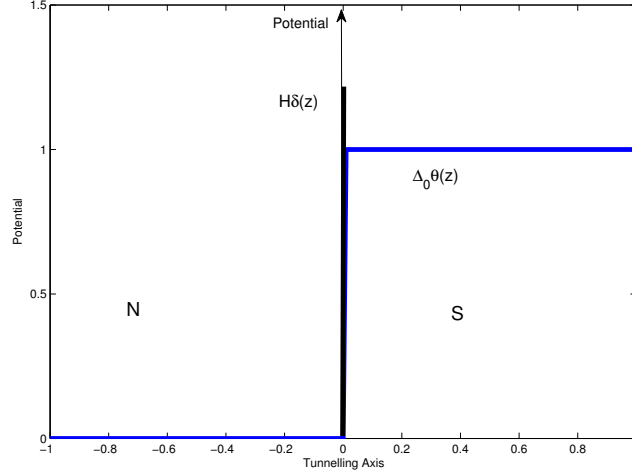


FIGURE 2.2: δ function of potential and step function of energy gap

particles and effective pair potential Δ_- felt by the hole-like particles as following

$$\Delta_{\pm} = |\Delta_{\pm}| \exp(i\phi_{\pm}) \quad (2.16)$$

From the analytical solutions of BdG equations, we obtain the kernel of (2.15), which is written in (2.17).

$$\sigma_R(E) = \frac{\sigma_S(E)}{\sigma_N} = \frac{1 + \sigma_N |\Gamma_+|^2 + (\sigma_N - 1) |\Gamma_+ \Gamma_-|^2}{|1 + (\sigma_N - 1) \Gamma_+ \Gamma_- \exp(i\phi_- - i\phi_+)|^2} \quad (2.17)$$

where the terms Γ_{\pm} , the normal conductance σ_N and the effective barrier height Z are

$$\Gamma_{\pm} = \frac{E - \sqrt{E^2 - |\Delta_{\pm}|^2}}{|\Delta_{\pm}|}, Z = \frac{Z_0}{\cos \theta}, \sigma_N = \frac{1}{1 + Z^2} \quad (2.18)$$

and we write the term $\sigma_S(E)$ for convenience.

$$\sigma_S(E) = \sigma_N \frac{1 + \sigma_N |\Gamma_+|^2 + (\sigma_N - 1) |\Gamma_+ \Gamma_-|^2}{|1 + (\sigma_N - 1) \Gamma_+ \Gamma_- \exp(i\phi_- - i\phi_+)|^2} \quad (2.19)$$

Fig.2.3 indicates different shapes with different, Z , the barrier height, where we assume that the phase difference $\phi_- - \phi_+ = 0$.

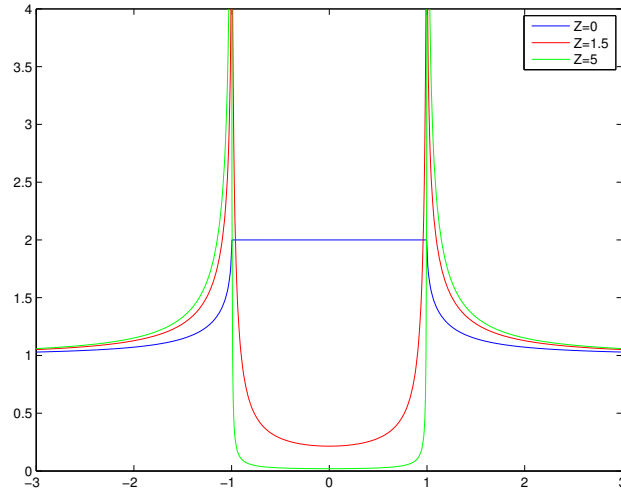


FIGURE 2.3: The picture indicates the different shapes of $\sigma_R(E)$ corresponding to the different barrier values. Here $\Delta_+ = \Delta_-$

The general function for the normalised tunnelling conductance σ_T is

$$\sigma_T(E) = \frac{\int d\Omega \sigma_S(E) \cos \theta}{\int d\Omega \sigma_N \cos \theta} \quad (2.20)$$

where we can see that the kernel σ_S is implemented. The integral operators in d -wave ab tunnelling and in c -tunnelling is written as

$$\begin{aligned} \int d\Omega^{(ab)} &= \int_{-\pi/2}^{\pi/2} d\theta \\ \int d\Omega^{(c)} &= \int_0^{2\pi} d\varphi \int_0^{\pi/2} d\theta \sin \theta \end{aligned} \quad (2.21)$$

φ is the interface angle.

2.2.3 ab -Tunnelling Spectroscopy

The d -wave tunnelling spectroscopy has are two cases: ab tunnelling whose tunnelling axis is normal to the c -axis of the crystal, and c tunnelling whose tunnelling axis is parallel to the c -axis of the crystal, Fig.2.1. We first of all discuss ab -tunnelling spectroscopy.

In fact, the averaged normal conductance in (2.20) can be derived directly.

$$\overline{\sigma_N} = \int d\Omega^{(ab)} \sigma_N \cos \theta \quad (2.22)$$

so that the averaged normal conductance is

$$\overline{\sigma}_N = 2 - \frac{Z_0}{\sqrt{1+Z_0^2}} \ln \left(\frac{\sqrt{1+Z_0^2} + 1}{\sqrt{1+Z_0^2} - 1} \right) \quad (2.23)$$

Now we focus our discussion on the specific case of $d_{x^2+y^2}$, where in ab -tunnelling Δ_- , Δ_+ are written as

$$\Delta_+ = \Delta_0 \cos 2(\theta - \alpha) \quad (2.24)$$

$$\Delta_- = \Delta_0 \cos 2(\theta + \alpha)$$

where θ represents incident angle, α the angle between the tunnelling axis and main axis of the pair potential, shown in Fig.2.4.

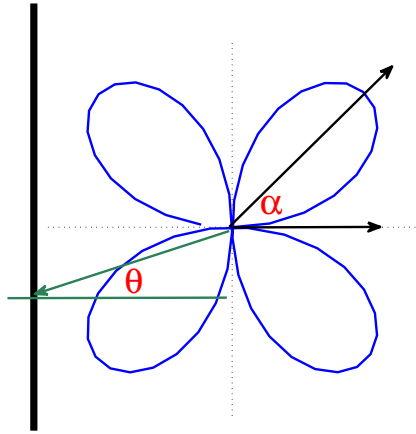


FIGURE 2.4: Schematic illustration of the incident angle θ and the angle α .

Turning to Fig.2.5, we see the shape of the conductance is sensitive to the incident angle and thus the phase difference

$$e^{i\phi_- - i\phi_+} = \frac{|\Delta_+|}{\Delta_+} \frac{\Delta_-}{|\Delta_-|} = \frac{|\cos 2(\theta - \alpha)|}{\cos 2(\theta - \alpha)} \frac{\cos 2(\theta + \alpha)}{|\cos 2(\theta + \alpha)|} \in \{-1, 1\} \quad (2.25)$$

Furthermore we limit the phase difference to zero.

Fig.2.6 shows the property of the ab tunnelling spectroscopy respect to different pair potentials, which indicates that one pair potential corresponds to one peak in the figure, while if pair potential is zero, the tunnelling conductance is a constant, 1.

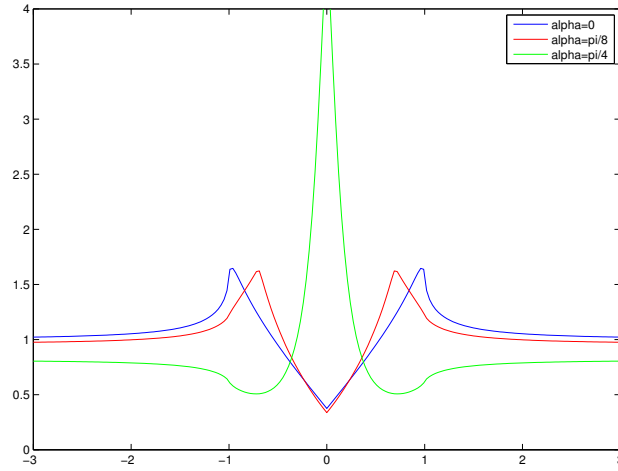


FIGURE 2.5: The figure indicates the correspondence of conductance and angle between incident normal and the petal axis.

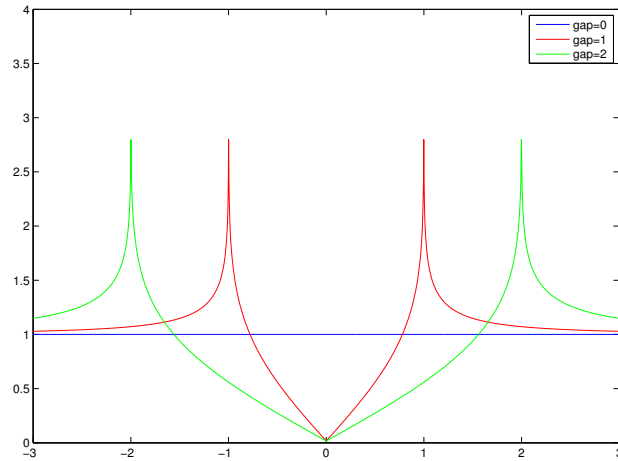


FIGURE 2.6: The figure demonstrates the total tunnelling conductance with different energy gaps. When energy gap amplitude is zero, the peaks vanish, meaning that the material turns into normal metal. Here we choose $Z = 5$

2.2.4 Differential Conductance with Different Temperatures and Fixed Energy Gap Amplitude

In general, the properties of differential conductance is determined by the derivative of the fermi function and tunnelling conductance kernel, according to (2.14) and (2.17). As an illustration, Fig. 2.7 shows differential conductance at Temperature 1K, where the top figure is the differential conductance, the bottom figure is the tunnelling conductance, and the others are the derivatives of fermi function at different biases. We see that the peak of the derivatives are close to δ functions, which makes the differential conductance look similar to the tunnelling conductance after the integration.

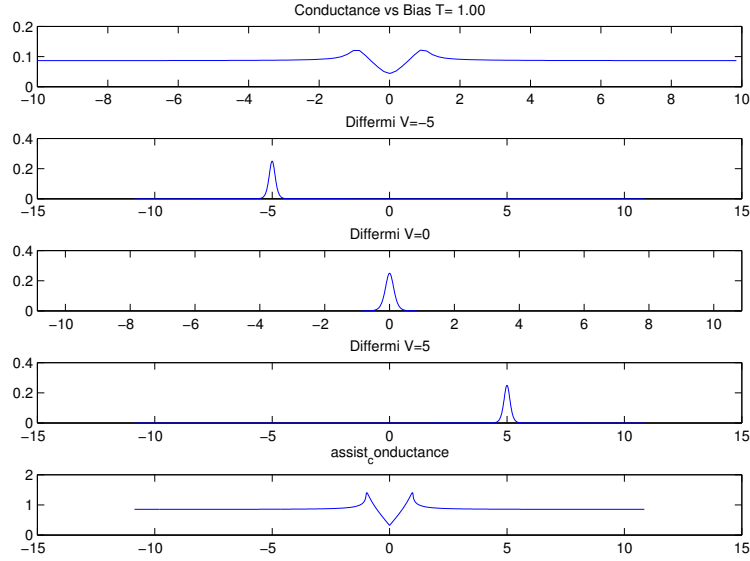


FIGURE 2.7: Differential conductance with $T=1K$, accompanied by plots of three derivatives of the fermi distributions at varied biases and a tunnelling conductance graph in the bottom.

Let's discuss a way to make the picture more clear in Fig.2.8, demonstrating the relation between the tunnelling conductance with temperature with a FIXED pair potential. We could observe that the dip in middle generally vanish as the temperature increases.

2.2.5 Differential Conductance with Different Pair Potential Amplitudes with Fixed Temperature

Though we should be clearly warned that the energy gap is dependent on the temperature, we still do a study for the relation between differential conductance with energy gap amplitudes.

Generally, the shapes of tunnelling conductance are similar except when the energy gap amplitude is zero, which will make the tunnelling conductance constant, already indicated in Fig.2.6.

Therefore, we simply provide an illustration figure. We could notice that with the increase energy gap amplitude, the centre dip becomes deeper, Fig.2.9.

Now we briefly introduce the calculation methods. It should be noted that we are trying to calculate a second order integral, which may lead to a large calculation time, as that we might have to calculate 1000×1000 volume. I developed a simple method based on

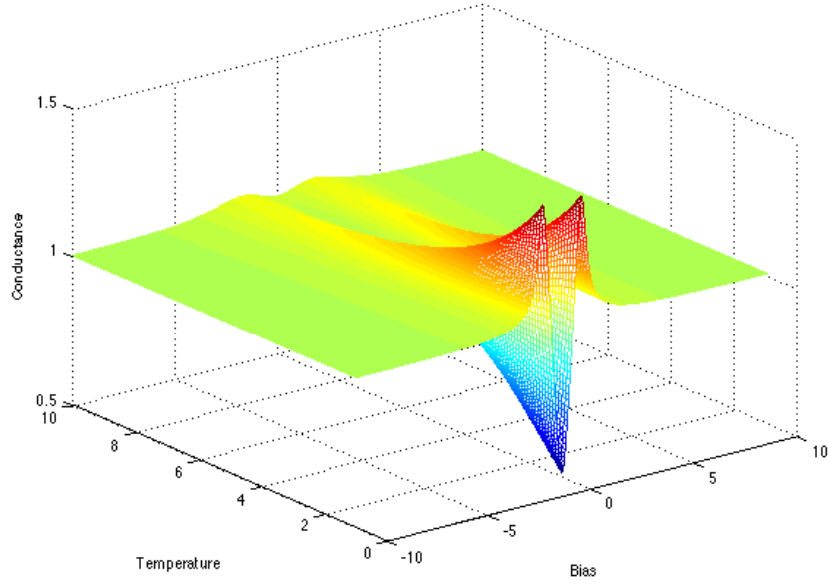


FIGURE 2.8: This figure indicates the relation between temperature, bias and the conductance. The different colours indicate the temperature.

the essential features of function σ_S and differential fermi distribution function $\frac{\partial f_0(E-eV)}{\partial V}$ in the integrations(2.14) and (2.20).

First of all, the function $\sigma_T(E)$ is assumed to be CONSTANT when parameter E 's absolute value is to some extent larger than amplitude of the energy gap, Fig.2.6.

Second, we note that differential fermi distribution function is actually of Delta function type, which means the value could be assumed zero when its parameter $E - \mu - eV$ is "much" larger than kT . Also, all the derivatives of the fermi distribution function shares the exact shape, shown in Fig.2.7; their only difference is that the peaks are in different positions corresponding to the value of bias.

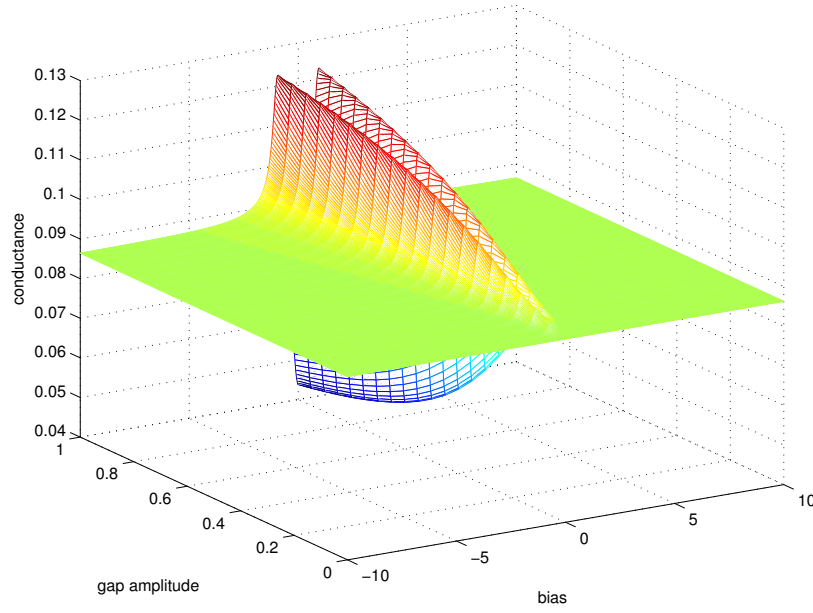


FIGURE 2.9: This figure indicates the relation between energy gap amplitude, bias and the conductance.

With the above knowledge, we calculate the the tunnelling spectroscopy point values according to a chosen step length ONLY ONCE and store the data. When parameter E is "large", we use constant for the point. We define this as calculation (1). Also, we calculate the point values of the derivative of the fermi distribution function at bias zero according to the step length used in the calculation (1). When parameter $E - \mu - eV$ is "large", we make the point value as zero. When We define this as calculation (2). Since calculation (1) and calculation (2) share the same step length, if we need to calculate the differential conductance at a certain bias, we translate the point values of the derivative to that bias and do the integration limited to the non-zero points of the derivative. To avoid losing information, the choice of the step length is significant. We choose step length according to the smaller value of peak width between the differential fermi distribution function and tunnelling conductance. The method remarkably improves the performance of the calculation yet loses very little accuracy. The weakness of this method is that the computation is slow when energy gap amplitude is small while the temperature is high, which, however, is easily to be removed by adding some plotting and integrating step boundaries.

2.2.6 c -Tunnelling Spectroscopy and Fitting the Experimental Data

As our experiments are conducted with the materials along c -axis of d-wave pair potential, we now focus on this case. The schematic illustration is shown in Fig.2.10. The

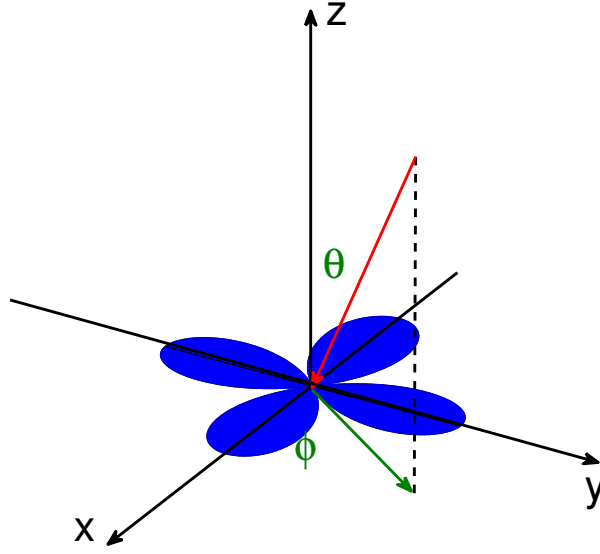


FIGURE 2.10: The schematic illustration of c -tunnelling, where the incident angle θ and the interface angle φ are indicated. In the figure, $x - y$ plane is the tunnelling interface.

pair potential in c -tunnelling is written as

$$\Delta(\varphi) = \Delta_0 \cos 2\varphi \quad (2.26)$$

The averaged N-I-N junction conductance over the half-sphere of k space could be calculated directly. According to the formula in the following, that calculates the averaged normal conductance,

$$\overline{\sigma_N} = \int_0^{2\pi} d\phi \int_0^{\frac{\pi}{2}} d\theta \cos \theta \sin \theta \sigma_N \quad (2.27)$$

where we assume that

$$\sigma_N = \frac{1}{1 + \left(\frac{Z_0}{\cos \theta}\right)^2} \quad (2.28)$$

We could simply calculate the integral for averaged normal conductance,

$$\overline{\sigma_N} = \pi \left[1 - Z_0^2 \ln \left(1 + \frac{1}{Z_0^2} \right) \right] \quad (2.29)$$

Knowing the formula (2.29), we could step over the numerical integral of normal conductance. Ideally, it also can be used to calculate the barrier height.

Typically the c -tunnelling spectroscopy is similar to that of ab -tunneling, when $\alpha = 0$, since the incident angle averages over the d -wave gap in a similar manner.

We conducted an experiment about the tunnelling spectroscopy with the layers of the material Bismuth strontium calcium copper oxide having the generalised chemical formula $Bi_2Sr_2Ca_{n-1}Cu_nO_{2n+4+x}$ (BSCCO) and Calcium doped Bi_2Se_3 (BSC), the former of which serves as a cuprate superconductor [12] and the latter of which serves as a topological insulator[13]. We use d -wave c -tunnelling model to fit the experimental data. Fig.2.11 shows the fitting results for our BSCCO on BSC experimental results by manually inputting the parameters.

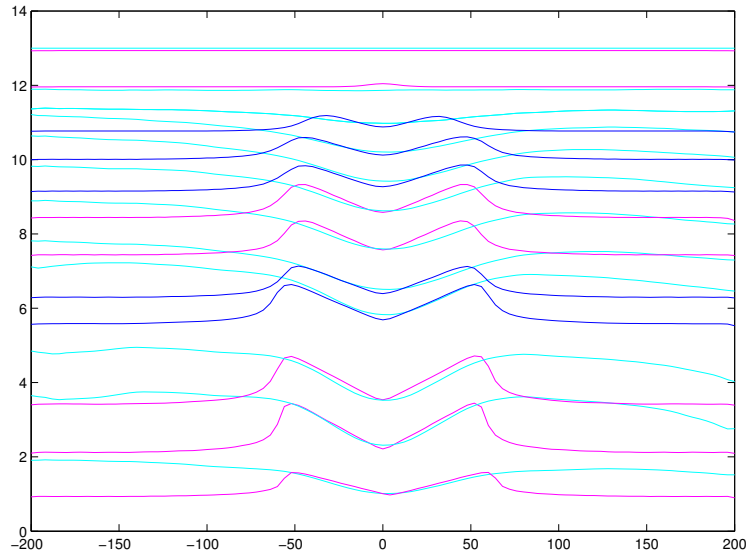


FIGURE 2.11: Conductances normalised by 70K with Temperature, where the deep colour represents calculation. Each bundle represents, from bottom to top, sequentially, 10K, 13K, 15K, 30K, 35K, 40K, 45K, 50K, 55K, 65K, 70K.

And chosen energy gaps versus temperature for fitting the experimental data are shown below, Fig.2.12.

The fitting results are not satisfactory. Only in the dip part the fitting results agree to some extent with the experimental results. But at the both sides they are quite far away. The reason for this disagreement is that the model we use is for low temperature case and is based on the assumption that the density of states is a constant at (2.12) and the properties of our model is determined by the integration kernel of (2.19), which also has peaks at the point $E = \Delta_0$. The experiment results, however, do not have the corresponding peaks, leading to the fact that the fitting results only match a small part of the experimental results in the centre.

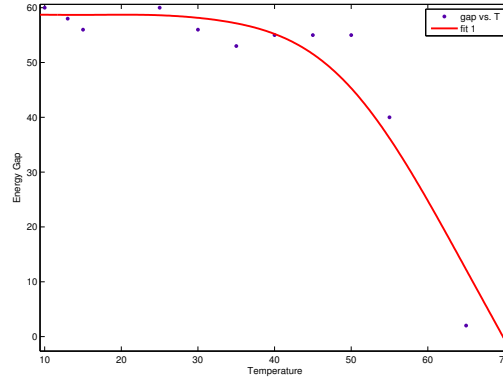


FIGURE 2.12: Energy Gaps with Temperature

To try to eliminate of the disagreement from the computational part, we implemented the genetic algorithm for fitting the data[14].

Genetic algorithm(GA) is an optimisation heuristic inspired by the natural selection process in biological systems. Very similar to the selection process, GA maintains a population of candidates and process mechanisms of encoding, selection, crossover, mutation and culling in the population[14].

In the calculation, we select a population of 50 for the desired parameters randomly generated within the set range and calculate the fitness value, such as standard error and then sort the population according to the fitness value increasingly. Second, we choose the first 25 of the population according to the sorted list as parents while we select another 25 samples of the population as mutants randomly multiplied by some restricted random numbers. 25 selected parents will generate 25 offsprings by crossover. Then we mix the original population, the generated offspring as well as the 25 mutants together to compose a country of 100 samples. Third, we do sorting again with the population the eliminate the last 50 samples of the population. We will repeat the above three steps until the termination requirement is satisfied.

The above statement is the ideal approach to fit the experimental data, while unfortunately the results come out not satisfactory.

Chapter 3

Tunnelling Spectroscopy with Proximity Effect

It is interesting to propose a theory calculating the d -wave conductance accounting for the proximity effect as required by our novel experiments. In this chapter, we limit our discussion to s -wave and $d_{x^2-y^2}$ cases.

Identical to the steps mentioned in the last chapter. We first solve the Bogoliubov equations and study the properties of the the tunnelling conductance kernel, σ_S in (2.25). Then the knowledge of the conductance kernel, σ_S will guide us to the desired d -wave proximity conductance. Currently this work is in progress.

3.1 Bogoliubov Equations

As a matter of fact, the tunnelling conductance discussed in the previous chapter is based on a specific case which is shown in Fig.2.2. The potential is assumed as a δ function and the pair potential is assumed as a step function, so that Bogoliubov equations(3.1) have an analytic solution. In contrast, such analytic solution no longer exists when dealing with more complicated case accounting for proximity effect where the gap is not simply a step function.

3.1.1 Simplification for the Bogoliubov Equations

The general Bogoliubov equations are

$$\begin{aligned} i\hbar \frac{\partial f}{\partial t} &= \left(-\frac{\hbar^2}{2m} \frac{\partial^2}{\partial z^2} - \mu(z) + V(z) \right) f(z, t) + \Delta(z) g(z, t) \\ i\hbar \frac{\partial g}{\partial t} &= \left(-\frac{\hbar^2}{2m} \frac{\partial^2}{\partial z^2} - \mu(z) + V(z) \right) g(z, t) + \Delta(z) f(z, t) \end{aligned} \quad (3.1)$$

Here we set z as our tunnelling axis. (3.1) has the solution form

$$\varphi(z, t) = \begin{pmatrix} f(z, t) \\ g(z, t) \end{pmatrix} \quad (3.2)$$

where $\mu(z), \Delta(z), V(z)$ are chemical potential, energy gap, and the ordinary potential which is related to the barrier height, in which we are interested in the latter two. By introducing a solution of the form in terms of the wave vector

$$\begin{aligned} f &= u(z) e^{i\mathbf{k}_F \cdot \mathbf{z} - \frac{iEt}{\hbar}} \\ g &= v(z) e^{i\mathbf{k}_F \cdot \mathbf{z} - \frac{iEt}{\hbar}} \end{aligned} \quad (3.3)$$

\mathbf{z} is the tunnelling axis vector. And \mathbf{k}_F represents the fermi vector, whose amplitude k_F is a CONSTANT for $d_{x^2-y^2}$ -wave case and s -wave case. And we relate it to the coherence length, another CONSTANT.

$$\xi_0 = \hbar v_F / (\pi \Delta_0) = \hbar^2 k_F / (\pi m \Delta_0) \quad (3.4)$$

The term Δ_0 is used in the expression (3.5) for s -wave and $d_{x^2-y^2}$ cases

$$\begin{aligned} \Delta(\mathbf{k}, z) &= \Delta_0 \Delta(z) \Delta(\mathbf{k}) \\ \Delta(z)|_{z=+\infty} &= 1, \Delta(z)|_{z=-\infty} = 0 \end{aligned} \quad (3.5)$$

We also define the following function for convenience

$$\Delta_\infty = \Delta(\mathbf{k}, +\infty) = \Delta(\mathbf{k}) \quad (3.6)$$

The Bogoliubov equations could be written in this way neglecting higher order terms[10].

$$\begin{aligned}\frac{\partial u}{\partial z} &= i(\pi\xi_0\Delta_0 \cdot (\hat{\mathbf{k}} \cdot \hat{\mathbf{z}}))^{-1}[Eu - \Delta(z)v] \\ \frac{\partial v}{\partial z} &= -i(\pi\xi_0\Delta_0 \cdot (\hat{\mathbf{k}} \cdot \hat{\mathbf{z}}))^{-1}[Ev - \Delta(z)u] \\ \hat{\mathbf{k}} &= \frac{\mathbf{k}}{|\mathbf{k}|}, \hat{\mathbf{z}} = \frac{\mathbf{z}}{|\mathbf{z}|}\end{aligned}\tag{3.7}$$

which are the equations we are interested in, ξ_0 is the coherence length. Also we have the accompanied boundary conditions taking into account the potential $V(z) = Z_0(\pi\xi_0\Delta_0)\delta(z)$

$$\begin{aligned}\varphi|_{z=0^+} &= \varphi|_{z=0^-} \\ \frac{\partial \varphi}{\partial z}\Big|_{z=0^+} - \frac{\partial \varphi}{\partial z}\Big|_{z=0^-} &= 2k_F Z_0 \varphi|_{z=0^+}\end{aligned}\tag{3.8}$$

As indicated in the reference[10], the Bogoliubov equations are solved region by region, which finally lead us to the tunnelling conductance kernel.

$$\sigma_S = 1 + A - B\tag{3.9}$$

The andreev reflection A and ordinary reflection B in (3.9) could be directly calculated from the solutions from the Bogoliubov equations.

3.1.2 Solving the Bogoliubov Equations

We divide the tunnelling axis into four regions, named 'super', 'reduced', 'induced', 'normal', respectively, which is shown in Fig.3.1, where we already choose parabolic shape for the pair potential. Now we solve the Bogoliubov equations region by region.

• 'Super' Region

In the 'super' region, we already know the solution in (3.10)-(3.12).

$$\begin{aligned}\varphi_1 &= \begin{pmatrix} u_0 \\ v_0 \end{pmatrix} e^{i(\mathbf{k}_F + \mathbf{k}'_S) \cdot \mathbf{z}} \\ \varphi_2 &= \begin{pmatrix} v_0 \\ u_0 \end{pmatrix} e^{-i(\mathbf{k}_F - \mathbf{k}'_S) \cdot \mathbf{z}}\end{aligned}\tag{3.10}$$

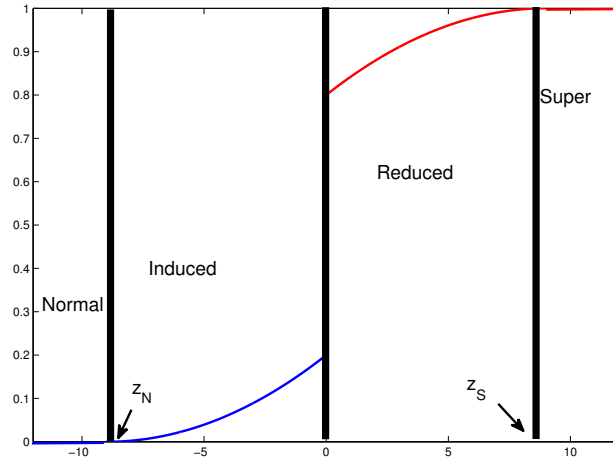


FIGURE 3.1: Parabolic shapes of reduced and induced pair potential. The tunnelling axis is divided into four regions.

where parameters are already known,

$$u_0^2 = 1 - v_0^2 = \frac{1}{2} \left(1 + \frac{(E^2 - \Delta_\infty^2)^{\frac{1}{2}}}{E} \right) \quad (3.11)$$

where Δ_∞ is defined in (3.6) and

$$k'_S = k_S / (\hat{\mathbf{k}} \cdot \hat{\mathbf{z}}) = (E^2 - \Delta_\infty^2)^{1/2} (\pi \xi_0 \Delta_0 (\hat{\mathbf{k}} \cdot \hat{\mathbf{z}}))^{-1} \quad (3.12)$$

The solution of this region serves as the generator of boundary conditions (3.14) for the solution of the next region, 'reduced' by applying the continuity of the wave functions φ and the derivative of the wave functions $\partial\varphi/\partial z$.

• **Reduced Region** The solution of reduced region is assumed to have the form (3.13).

$$\varphi_j = \begin{pmatrix} u_{aj} \\ v_{aj} \end{pmatrix} e^{i\mathbf{k}_F \cdot \mathbf{z}} + \begin{pmatrix} v_{bj} \\ u_{bj} \end{pmatrix} e^{-i\mathbf{k}_F \cdot \mathbf{z}}, j = 1, 2 \quad (3.13)$$

Realising that $\mathbf{k}'_S \cdot \mathbf{z} = k_S / \cos \theta \hat{\mathbf{k}} \cdot \hat{\mathbf{z}} = k_S z$ according to (3.12), the boundary condition for the reduced region is

$$\begin{aligned} u_{a1}(z_S) &= u_{b2}(z_S) = u_0 e^{ik_S z_S} \\ v_{a1}(z_S) &= v_{b2}(z_S) = v_0 e^{ik_S z_S} \end{aligned} \quad (3.14)$$

$$u_{b1}(z_S) = u_{a2}(z_S) = 0$$

$$v_{b1}(z_S) = v_{a2}(z_S) = 0$$

The term z_S and z_N are shown in Fig.3.1 and indicate the boundary of the reduced region with the super region and the normal region with the induced region respectively. After obtaining the numerical solutions for (3.13), we select the values of only one point, which is at $z = 0$

$$u_{a1}(0) = u_{b2}(0) = u_{a1}^+ \quad (3.15)$$

$$v_{a1}(0) = v_{b2}(0) = v_{a1}^+$$

Before we move to the induced region, we make use of the original boundary condition at $z = 0$, setting $V(z) = Z_0(\pi\xi_0\Delta_0)\delta(z)$. In the boundary conditions (3.16), the symbols $+$, $-$ represent $z = 0^+$, $z = 0^-$, respectively.

$$\varphi|_{z=0^+} = \varphi|_{z=0^-} \quad (3.16)$$

$$\left. \frac{\partial \varphi}{\partial z} \right|_{z=0^+} - \left. \frac{\partial \varphi}{\partial z} \right|_{z=0^-} = 2k_F Z_0 \varphi|_{z=0^+}$$

We neglect terms $u_{b1}(z)$, $u_{a2}(z)$, $v_{b1}(z)$, $v_{a2}(z)$ as they are zero because they have 0 initial values in (3.14).

• **Induced Region** In light of the boundary conditions (3.16), we write the solution of the induced region in the form of

$$\begin{aligned} \varphi_1 &= (1 + iZ) \begin{pmatrix} u_{a0} \\ v_{a0} \end{pmatrix} e^{i\mathbf{k}_F \cdot \mathbf{z}} - iZ \begin{pmatrix} v_{b0} \\ u_{b0} \end{pmatrix} e^{-i\mathbf{k}_F \cdot \mathbf{z}} \\ \varphi_1 &= iZ \begin{pmatrix} u_{b0} \\ v_{b0} \end{pmatrix} e^{i\mathbf{k}_F \cdot \mathbf{z}} + (1 - iZ) \begin{pmatrix} v_{a0} \\ u_{a0} \end{pmatrix} e^{-i\mathbf{k}_F \cdot \mathbf{z}} \\ Z &= \frac{Z_0}{\widehat{\mathbf{k}} \cdot \widehat{\mathbf{z}}} \end{aligned} \quad (3.17)$$

Then the boundary conditions for the induced region are expressed in (3.18).

$$u_{a0}^- = u_{a1}^+, v_{a0}^- = v_{a1}^+ \quad (3.18)$$

$$u_{b0}^- = v_{a1}^+, v_{b0}^- = u_{a1}^+$$

• **Normal Region** After the induced solution is numerically obtained, we again choose the value only at $z = -z_N$, which is the interface of induced region and normal region.

$$\begin{aligned} u_a &= u_{a0}(-z_N), v_a = v_{a0}(-z_N) \\ u_b &= u_{b0}(-z_N), v_b = u_{b0}(-z_N) \end{aligned} \quad (3.19)$$

The solution in the normal region has the form (3.20), noting that we already make wave vectors parallel to the incident.

$$\begin{aligned} \varphi_j &= \nu_j \left[\begin{pmatrix} 1 \\ 0 \end{pmatrix} e^{i(k_F+k_N)z} + a_e \begin{pmatrix} 0 \\ 1 \end{pmatrix} e^{i(k_F-k_N)z} + b_e \begin{pmatrix} 1 \\ 0 \end{pmatrix} e^{-i(k_F+k_N)z} \right] \\ &+ \eta_j \left[\begin{pmatrix} 0 \\ 1 \end{pmatrix} e^{-i(k_F-k_N)z} + a_h \begin{pmatrix} 1 \\ 0 \end{pmatrix} e^{-i(k_F+k_N)z} + b_h \begin{pmatrix} 0 \\ 1 \end{pmatrix} e^{i(k_F-k_N)z} \right] \end{aligned} \quad (3.20)$$

The coefficients in (3.17) could again be obtained by applying the the continuity.

$$\begin{aligned} a_e &= \frac{(1+Z^2)u_a v_a - Z^2 u_b v_b}{(1+Z^2)u_a^2 - Z^2 u_b^2} e^{-2ik_N z_N} \\ b_e &= \frac{iZ(1-iZ)(u_b v_a - u_a v_b)}{(1+Z^2)u_a^2 - Z^2 u_b^2} e^{-2ik_N z_N} \end{aligned} \quad (3.21)$$

So that the tunnelling conductance kernel versus energy is written as

$$\sigma_S = 1 + A - B = 1 + |a_e|^2 - |b_e|^2 \quad (3.22)$$

3.2 Properties of Tunnelling Spectroscopy Kernel with Proximity Effect at Normal Incident

Under the condition of the normal incident, $\hat{\mathbf{k}} \cdot \hat{\mathbf{z}} = 1$.

3.2.1 The Shapes of Reduced and Induced Pair Potential

To be precise we need to compute the pair potential using self-consistent method[15]. Yet we won't lose too much information if we only guess the shape of the pair potential[3, 10]. We are using parabolic shape of pair potential which is like Fig.3.1

Another point we should account for is the proximity thickness, which will affect much the shape of the computed results. We define

$$z_S = a_S \pi \xi_0, z_N = a_N \pi \xi_0, \xi_0 = \hbar^2 k_F / (\pi m \Delta_0) \quad (3.23)$$

where in effect we find the factors a_S, a_N play the role of influencing the results. Therefore, we choose the potential function as

$$\begin{aligned} \Delta_R(\mathbf{k}, z) &= \frac{\Delta_r(\mathbf{k}) - \Delta_\infty}{z_S^2} (z - z_S)^2 + \Delta_\infty(\mathbf{k}) \\ \Delta_I(\mathbf{k}, z) &= \frac{\Delta_i(\mathbf{k})}{z_N^2} (z + z_S)^2 \end{aligned} \quad (3.24)$$

who have the shapes in 3.1. The terms Δ_r, Δ_i represents the reduced gap and induced gap, respectively. Since it is in s -wave in the current discussion, the terms appearing in (3.24) are all independent of \mathbf{k} space.

3.2.2 Specific Cases

We check the reliability of our model by calculating the specific cases of the tunnelling kernel(3.9). In the following we set $\Delta_0 = 1$ in (3.5).

First, BTK is a special case of proximity effect; in other words, if we set $\Delta_R = 1, \Delta_I = 0$, we should see the results of BTK, Fig.3.2. Fig.3.2 compares the plots generated from the formula (2.17) and from solving the Bogoliubov equations discussed in the last section. We calculate the tunnelling conductance for various barrier heights and see the two results match quite well.

Also, when barrier height $Z_0 = 0$, we should observe flat region with the value of 2 in the middle, Fig.3.3.

3.2.3 s -wave Proximity Effect at Normal Incident with Various Parameters

Similar to the procedure in the previous chapter, with solutions obtained, we first have a look at the kernel of the conductance, σ_S , in (3.9).

We draw a list of figures showing the change of the shape according to the varying reduced gap and induced gap, setting the coherence length as $\pi \xi_0 = 1$, Fig.3.4-Fig.3.6.

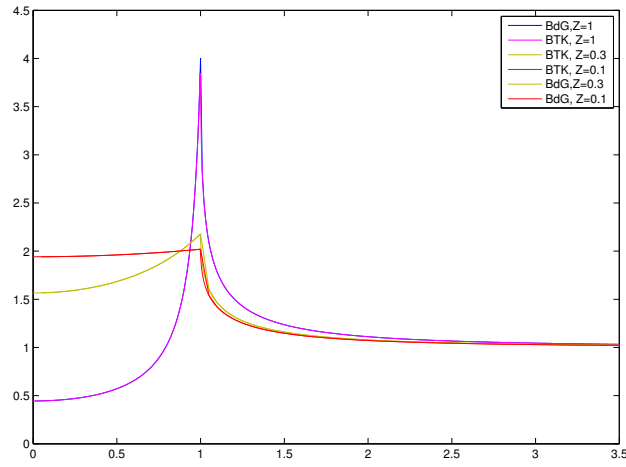
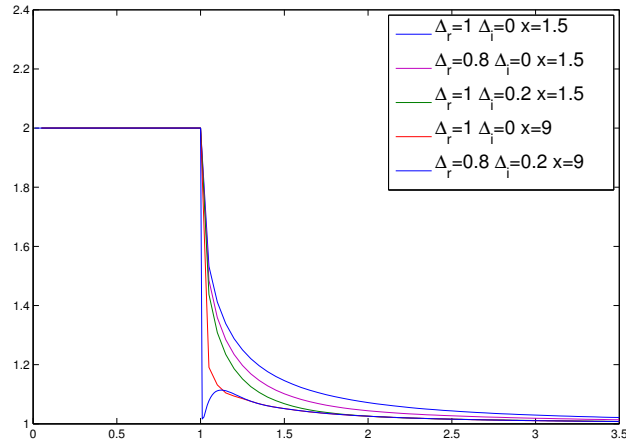
FIGURE 3.2: BTK case when we set $\Delta_R = 1, \Delta_I = 0$ 

FIGURE 3.3: The flat region in the middle appears no matter what reduced gap and induced gap and the proximity region thickness are

Also, as a thought, the proximity region width scaled on the coherence length may affect the transmission. Comparing the plots in Fig.3.7 or comparing Fig.3.4 with Fig.3.5, we can discover the difference. The thicker proximity region leads to the higher conductance value close to $E = 0$ and create more peaks.

The Fig.3.8 and Fig.3.9 gives us a clearer picture of the existence of the reduced gap and induced gap.

In Fig.3.8, we set bulk gap $\Delta_0 = 2$, fix the reduced gap $\Delta_r = 1$ and vary the induced gap Δ_i from 0 to 1.5. The red tongue in the middle indicates the properties of the varying

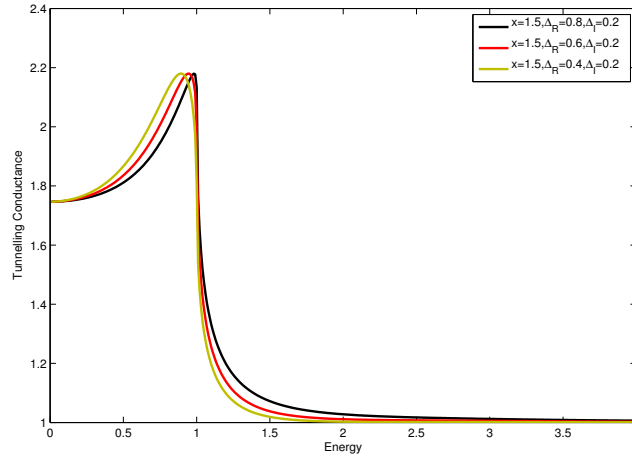


FIGURE 3.4: Low barrier height $Z_0 = 0.3$ for various values of the reduced gap. We don't see many peaks when the proximity region is thin.

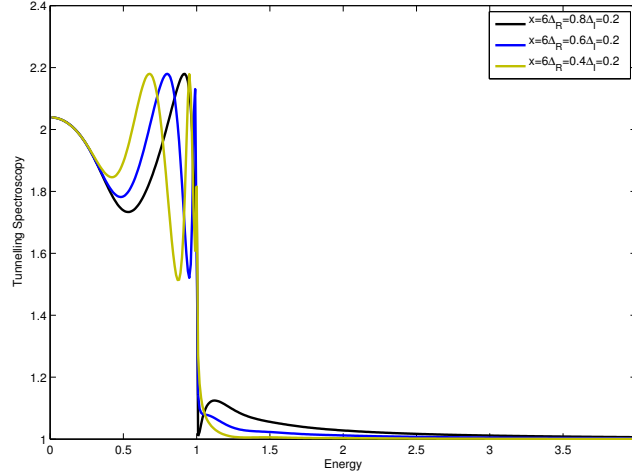


FIGURE 3.5: Some peaks show if thicker proximity region is chosen at low barrier height, with reduced gap varying and included gap fixed. $Z_0 = 0.3$.

induced gap, whose width is from 0 to about 1.5, corresponding to the value of induced gap at that point.

In Fig.3.9, we set bulk gap $\Delta_0 = 2$, fix the induced gap $\Delta_i = 0.4$ and vary the reduced gap Δ_r from 0 to 2. The red rectangular with *width* = 0.8 shows the existence of the induced gap. The two branches growing from the bottom indicates the existence of the reduced gap. The minimum value of the reduced gap in the bottom seems to be expelled by the induced gap that it could not reach 0 as it should be. The maximum value of the reduced gap is at 1 as it should be.

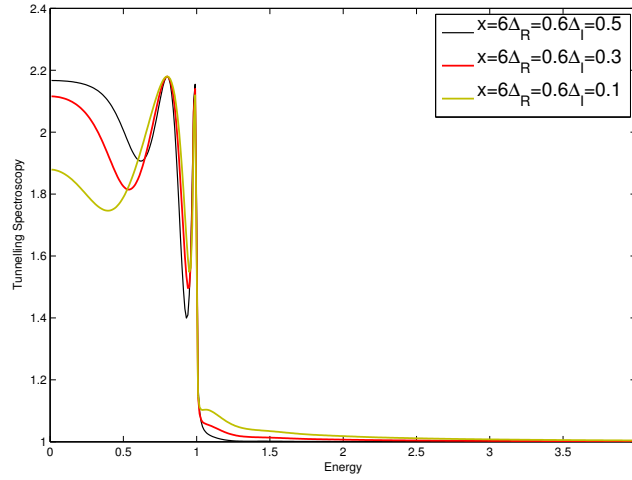


FIGURE 3.6: Some peaks show if thicker proximity region is chosen at low barrier height, with induced gap varying and reduced gap fixed. $Z_0 = 0.3$.

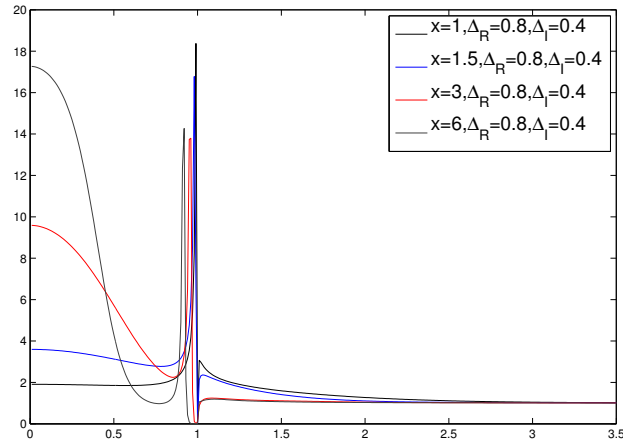


FIGURE 3.7: Increasing the proximity thickness leads to increasing value in the middle and create more peaks. $Z_0 = 3$

3.3 An In Progress Approach to the *d*-wave Tunnelling Spectroscopy with Proximity Effect

In the *d*-wave tunnelling case, the transmission and reflection is interpreted in Fig 3.10. Note that the wave-vector parallel to the interface are always conserved. For the wave-vectors in the incident plane, we assume that

$$|\mathbf{k}_N^e| = |\mathbf{k}_S^e| \quad (3.25)$$

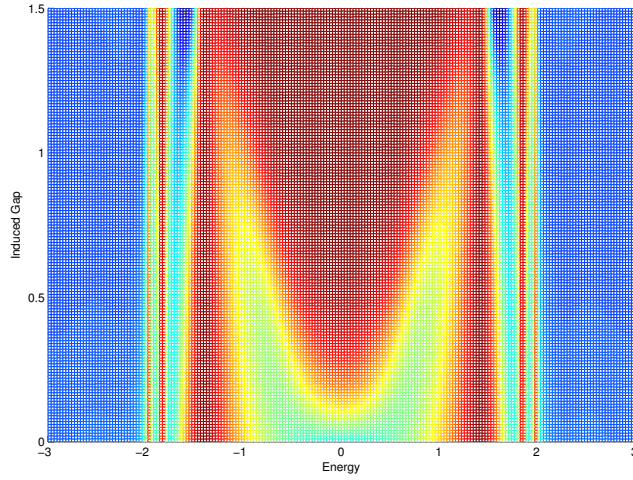


FIGURE 3.8: The picture shows the properties of the tunnelling conductance when induced gap is varying while reduced gap is fixed. The blue colour indicates the low conductance value while in contrast the red colour indicates the high conductance value.

According to the momentum conservation law for its interface component,

$$|\mathbf{k}_N^e| \sin \theta_N = |\mathbf{k}_S^e| \sin \theta_S \quad (3.26)$$

so that

$$\begin{aligned} \theta_S &= \theta_N = \theta \\ \mathbf{k}_N^e &= \mathbf{k}_S^e \end{aligned} \quad (3.27)$$

We use \mathbf{k} to express the incident and transmission wave-vectors. In d -wave case, the Bogoliubov equations are written as [15].

$$\begin{aligned} \frac{\partial u}{\partial z} &= i(\pi \xi_0 \Delta_0 \cos \theta)^{-1} [Eu - \Delta(z)v] \\ \frac{\partial v}{\partial z} &= -i(\pi \xi_0 \Delta_0 \cos \theta)^{-1} [Ev - \Delta(z)u] \\ \mathbf{k} \cdot \mathbf{z} &= \cos \theta \end{aligned} \quad (3.28)$$

And in addition we write another organised Bogoliubov equations for analysis,

$$\begin{aligned} \frac{\partial^2 u}{\partial z^2} - \frac{1}{\Delta} \frac{\partial \Delta}{\partial z} \frac{\partial u}{\partial z} + \left(\frac{i}{B\Delta} \frac{\partial \Delta}{\partial z} E + \frac{E^2 - \Delta^2}{B^2} \right) u &= 0 \\ \frac{\partial^2 v}{\partial z^2} - \frac{1}{\Delta} \frac{\partial \Delta}{\partial z} \frac{\partial v}{\partial z} + \left(-\frac{i}{B\Delta} \frac{\partial \Delta}{\partial z} E + \frac{E^2 - \Delta^2}{B^2} \right) v &= 0 \\ B &= \pi \xi_0 \Delta_0 \cos \theta \end{aligned} \quad (3.29)$$

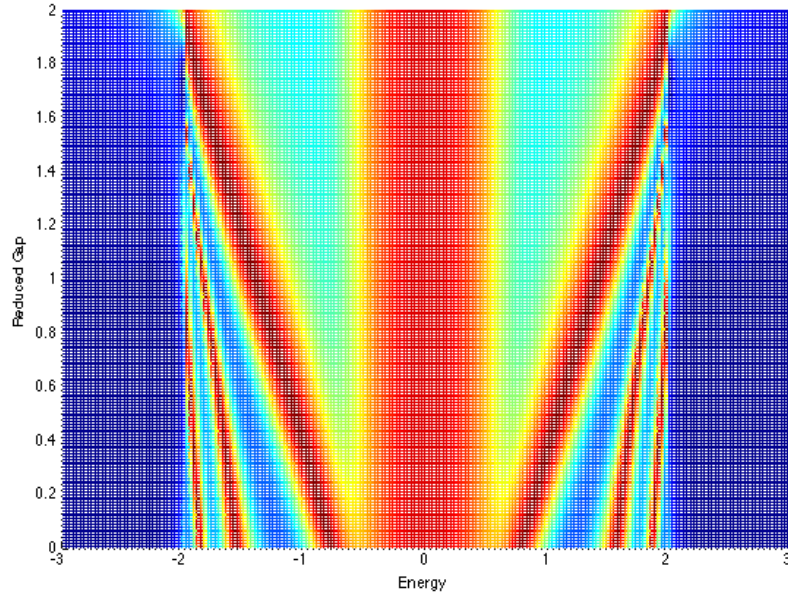


FIGURE 3.9: The picture shows the properties of the tunnelling conductance when the reduced gap is varying while the induced gap is fixed. The blue colour indicates the low conductance value while in contrast the red colour indicates the high conductance value.

After obtaining the u, v values for each incident angle θ and interface angle ϕ , we refer to the formulae (2.20) and (2.21).

Again to make sure the model is correct, we attempt to reproduce d -wave BTK here. In the case of BTK, we could directly write the terms (3.19) as

$$\begin{aligned}
 z_N &= z_S = 0 \\
 u_a &= u_0 e^{ik_S z_S}, v_a = v_0 e^{ik_S z_S} \\
 u_b &= v_0 e^{ik_S z_S}, v_b = u_0 e^{ik_S z_S}
 \end{aligned} \tag{3.30}$$

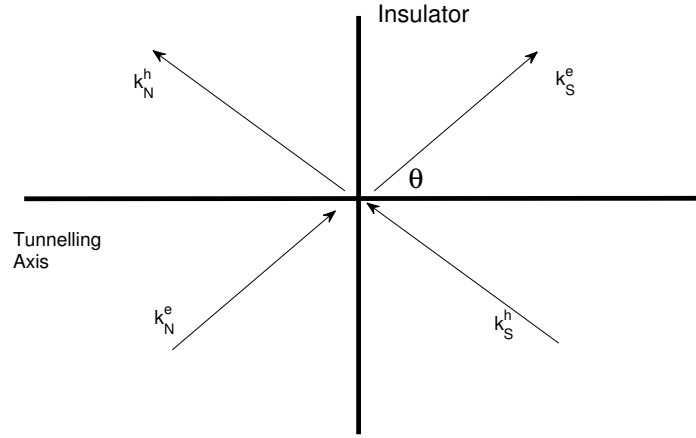


FIGURE 3.10: The four processes happen at the insulator. k_S^e is the ordinary electron reflection vector; k_S^h is the hole reflection vector; k_N^e is the electron transmission vector; k_N^h is the hole transmission vector.

so that the Andreev reflection a_e and the ordinary reflection b_e is can be derived,

$$|a_e| = \left| \frac{u_0 v_0}{(1 + Z^2)u_0^2 - Z^2 v_0^2} \right| \quad (3.31)$$

$$|b_e| = \left| \frac{iZ(1 - iZ)(v_0^2 - u_0^2)}{(1 + Z^2)u_0^2 - Z^2 v_0^2} \right|$$

Note that (3.31) is identical to (2.19), if we set phase difference of the pair potentials as 0.

We take a look at the ab -tunnelling first. Please be aware that in ab -tunnelling we DID NOT place the factor $\cos \theta$ in the equation (3.28) for the specific case of BTK indicated by the reference[5]. This is mathematically derived from the above statements about BTK case, that the factor $\pi \xi_0 \Delta_0 \cos \theta$ is trivial in the BTK case as the reduced region and induced region don't exist, leading to the fact that the solution is irrelevant to this factor. As indicated in the previous chapter, the pair potential related both to momentum space and position space has the form

$$\Delta(\theta, z) = |\Delta(z) \cos 2\theta| \quad (3.32)$$

where $\Delta(z)$ can be referred to (3.24). Also we choose the absolute value of the pair potential according to the (3.29). In Fig.3.11, we could see that the reproduction is fine.

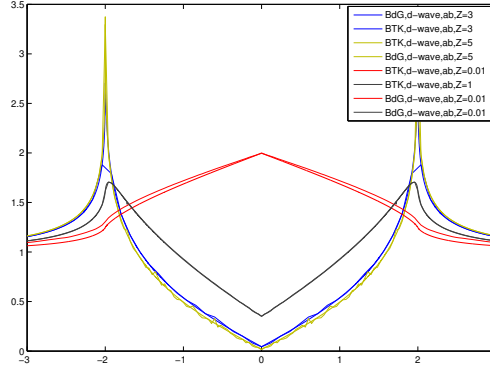


FIGURE 3.11: The reproduction for the $d_{x^2-y^2}$ ab -tunnelling case. $Z_0 = 0.01, 1, 3, 5$

In c -axis tunnelling in which we are more interested, we set pair potential as

$$\Delta(\varphi, z) = |\Delta(z) \cos 2\varphi| \quad (3.33)$$

It can be derived from (2.5). In Fig.3.12, we could see that the reproduction is fine.

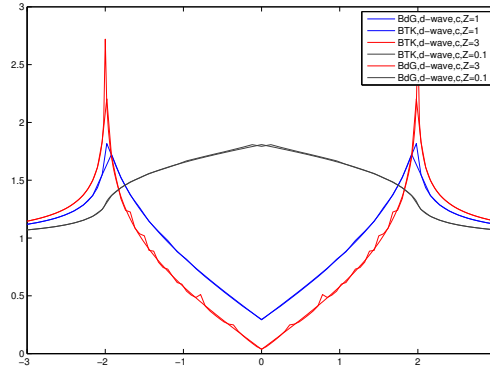


FIGURE 3.12: The reproduction for the $d_{x^2-y^2}$ c -tunnelling case. $Z_0 = 0.1, 1, 3$

We are still working on the d -wave proximity tunnelling spectroscopy. We did a trial calculation for the d -wave ab -tunnelling case. In the calculation, the $\cos \theta$ in (3.28) is no longer trivial. Also, we can draw the conclusion from (3.28) that if tunnelling at large incident angle, close to $\pm\pi/2$, the functions $u(z), v(z)$ will oscillate heavily. Meanwhile, $\cos \theta$ in the integral formula (2.20) is relatively small, in the light of which we do not have to do a complete half sphere integration, but within the domain $\theta \in [-1.5, 1.5]$, so that a faster computation might be performed. Fig.3.13 shows the proximity tunnelling conductance, the induced gap is clearly identified by the bulk in the centre. And the reduced gap is indicated by the second peak whose value, however is slightly larger than

the reduced gap value. Also, as the figure is plotted in low resolution, we see some unwanted peaks around the bulk gap. Or it might be caused by the resonance due to thick proximity domain. Fig.3.14 shows the proximity tunnelling conductance with various reduced gaps and induced gaps. We can observe that with the same induced gap, the plots share the same bulk in the middle, similar to the figures of normal incident kernel Fig.3.4-Fig.3.6. Fig.3.14 shows additional plots for comparison.

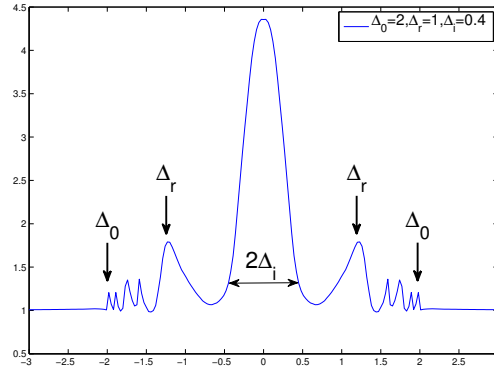


FIGURE 3.13: The tunnelling conductance with bulk gap $\Delta_0 = 2$, reduced gap $\Delta_r = 1$, $\Delta_i = 0.4$, which are indicated in the figure. We can see that at the bulk gap side there are some oscillations, which may be due to the resolution of the calculation. $Z_0 = 1$

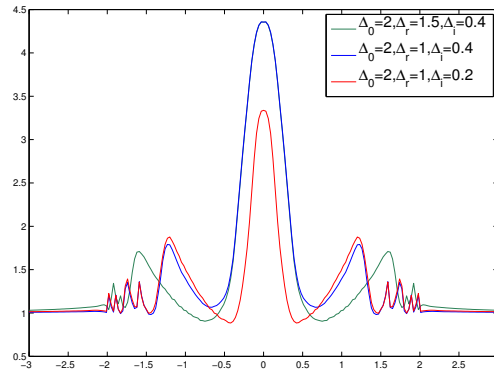


FIGURE 3.14: The tunnelling conductance with various reduced gaps and induced gaps. $Z_0 = 1$.

Now we approach the *d*-wave *c*-tunnelling conductance. Similar to the case of *ab*-tunnelling, we conduct the integration within the domain $\varphi \in [0, 2\pi], \theta \in [0, 1.5]$. Fig.3.15 shows the proximity tunnelling conductance, the induced gap is clearly identified by the bulk in the centre. And the reduced gap is indicated by the second peak whose value, however is slightly larger than the reduced gap value. The shape of *c*-tunnelling

conductance is quite similar to that of *ab*-tunnelling. Fig.3.16 shows additional plots for comparison.

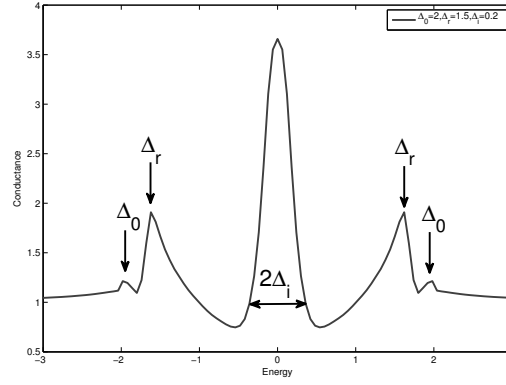


FIGURE 3.15: The tunnelling conductance with bulk gap $\Delta_0 = 2$, reduced gap $\Delta_r = 1.5$, $\Delta_i = 0.2$, which are indicated in the figure. $Z_0 = 1$

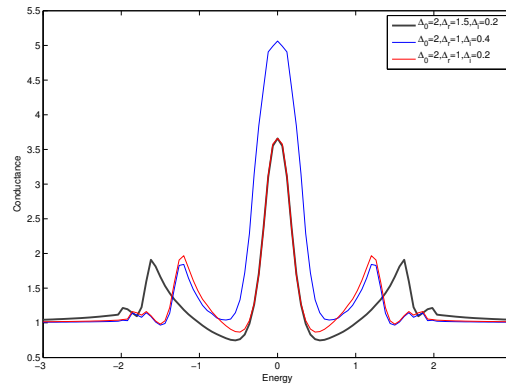


FIGURE 3.16: The tunnelling conductance with various reduced gaps and induced gaps. $Z_0 = 1$.

Chapter 4

Future Work

We conclude our work of calculating d -wave tunnelling spectroscopy and fitting the experimental data as well as the calculation the tunnelling spectroscopy accounting for proximity effect.

For the work described in Chapter 2, first of all we need to modify our model. As stated at the end of Chapter 2, the density of states is assumed to be constant, which might probably not be true. Also, we need to perform a calculation using genetic algorithm which is more reliable.

For the work calculating the proximity effect, though it reproduces quite well for the special cases, the picture of reduced gap and induced gap is blurred; we do not have a clear idea of what their effects are. Moreover, we need to have a deeper study of the d -wave tunnelling spectroscopy with proximity effect.

Chapter 5

Additional Projects

5.1 Control System for Raman Stage and Fresnel Rhomb

The software I designed integrates the XYZ stage control panel and the Fresnel Rhomb control panel. Users can operate XYZ stage and the Fresnel Rhomb at the same time with convenience. For XYZ stage control part, apart from controlling the stage, users can store the positions of their samples that may be studied later. For Fresnel control part, the digits shown on the software are really polarization angles so that users do not need to convert the units. In addition, a polarization clock is provided to assist the operation. What is more, the COM interface is also adjustable even in the case that the software is installed in a substituted computer.

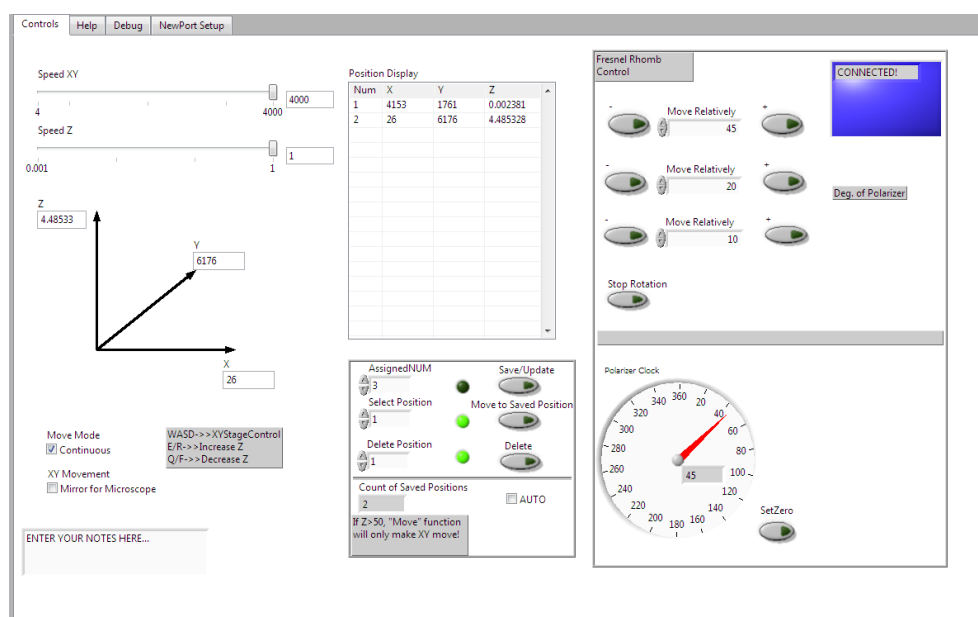


FIGURE 5.1: Main Control Panel

Bibliography

- [1] G. E. Blonder, M. Tinkham, and T. M. Klapwijk, “Transition from metallic to tunneling regimes in superconducting microconstrictions: Excess current, charge imbalance, and supercurrent conversion,” *Phys. Rev. B*, vol. 25, pp. 4515–4532, Apr 1982.
- [2] S. Guéron, H. Pothier, N. O. Birge, D. Esteve, and M. H. Devoret, “Superconducting proximity effect probed on a mesoscopic length scale,” *Phys. Rev. Lett.*, vol. 77, pp. 3025–3028, Sep 1996.
- [3] D. R. Heslinga, S. E. Shafranjuk, H. van Kempen, and T. M. Klapwijk, “Observation of double-gap-edge andreev reflection at si/nb interfaces by point-contact spectroscopy,” *Phys. Rev. B*, vol. 49, pp. 10484–10494, Apr 1994.
- [4] S. Guéron, H. Pothier, N. O. Birge, D. Esteve, and M. H. Devoret, “Superconducting proximity effect probed on a mesoscopic length scale,” *Phys. Rev. Lett.*, vol. 77, pp. 3025–3028, Sep 1996.
- [5] S. Kashiwaya, Y. Tanaka, M. Koyanagi, and K. Kajimura, “Theory for tunneling spectroscopy of anisotropic superconductors,” *Phys. Rev. B*, vol. 53, pp. 2667–2676, Feb 1996.
- [6] Y. Tanaka and S. Kashiwaya, “Theory of tunneling spectroscopy of d -wave superconductors,” *Phys. Rev. Lett.*, vol. 74, pp. 3451–3454, Apr 1995.
- [7] Y. Tanaka and S. Kashiwaya, “Theory of tunneling spectroscopy of d -wave superconductors,” *Phys. Rev. Lett.*, vol. 74, pp. 3451–3454, Apr 1995.
- [8] O. Millo, I. Asulin, O. Yuli, I. Felner, Z.-A. Ren, X.-L. Shen, G.-C. Che, and Z.-X. Zhao, “Scanning tunneling spectroscopy of smfeaso_{0.85}: Possible evidence for d -wave order-parameter symmetry,” *Phys. Rev. B*, vol. 78, p. 092505, Sep 2008.
- [9] W. K. Park, L. H. Greene, J. L. Sarrao, and J. D. Thompson, “Andreev reflection at the normal-metal/heavy-fermion superconductor CeCoIn₅ interface,” *Phys. Rev. B*, vol. 72, p. 052509, Aug 2005.

-
- [10] P. C. van Son, H. van Kempen, and P. Wyder, “Andreev reflection and geometrical resonance effects for a gradual variation of the pair potential near the normal-metal \sim superconductor interface,” *Phys. Rev. B*, vol. 37, pp. 5015–5023, Apr 1988.
 - [11] C. Bruder, “Andreev scattering in anisotropic superconductors,” *Phys. Rev. B*, vol. 41, pp. 4017–4032, Mar 1990.
 - [12] M. F. Hiroshi Maeda, Yoshiaki Tanaka and T. Asano, “A new high- t_c oxide superconductor without a rare earth element,” *Jpn. J. Appl. Phys*, vol. 27, pp. L209–L210, January 1988.
 - [13] D. Q. D. Hsieh, Y. Xia, “A tunable topological insulator in the spin helical dirac transport regime,” *Nature*, vol. 460, pp. 1101–1105, August 2009.
 - [14] A. S. M. Gulsen and D. Tale, “A genetic algorithm approach to curve fitting,” *INT. J. PROD. RES*, vol. 33, pp. 1911–1923, July 1995.
 - [15] C. Bruder, “Andreev scattering in anisotropic superconductors,” *Phys. Rev. B*, vol. 41, pp. 4017–4032, Mar 1990.